



# The effect of pore size on the mechanical properties, biodegradation and osteogenic effects of additively manufactured magnesium scaffolds after high temperature oxidation: An *in vitro* and *in vivo* study

Chaoxin Wang<sup>a,b,1</sup>, Jinge Liu<sup>c,1</sup>, Shuyuan Min<sup>a,b</sup>, Yu Liu<sup>a,b</sup>, Bingchuan Liu<sup>a,b</sup>, Yuanyu Hu<sup>a,b</sup>, Zhengguang Wang<sup>a,b</sup>, Fengbiao Mao<sup>d</sup>, Caimei Wang<sup>e</sup>, Xiaolin Ma<sup>e</sup>, Peng Wen<sup>c,\*\*</sup>, Yufeng Zheng<sup>f,\*\*\*</sup>, Yun Tian<sup>a,b,\*</sup>

<sup>a</sup> Department of Orthopedics, Peking University Third Hospital, Beijing, 100191, China

<sup>b</sup> Engineering Research Center of Bone and Joint Precision Medicine, Ministry of Education, Beijing, 100191, China

<sup>c</sup> Department of Mechanical Engineering, Tsinghua University, Beijing, 100084, China

<sup>d</sup> Institute of Medicine Innovation and Research, Peking University Third Hospital, Beijing, 100191, China

<sup>e</sup> Beijing AKEC Medical Co., Ltd., Beijing, 102200, China

<sup>f</sup> School of Materials Science and Engineering, Peking University, Beijing, 100871, China

## ARTICLE INFO

### Keywords:

Pore size  
Additive manufacturing  
WE43 alloy  
Magnesium alloy

## ABSTRACT

The effects of pore size in additively manufactured biodegradable porous magnesium on the mechanical properties and biodegradation of the scaffolds as well as new bone formation have rarely been reported. In this work, we found that high temperature oxidation improves the corrosion resistance of magnesium scaffold. And the effects of pore size on the mechanical characteristics and biodegradation of scaffolds, as well as new bone formation, were investigated using magnesium scaffolds with three different pore sizes, namely, 500, 800, and 1400  $\mu\text{m}$  (P500, P800, and P1400). We discovered that the mechanical characteristics of the P500 group were much better than those of the other two groups. *In vitro* and *in vivo* investigations showed that WE43 magnesium alloy scaffolds supported the survival of mesenchymal stem cells and did not cause any local toxicity. Due to their larger specific surface area, the scaffolds in the P500 group released more magnesium ions within reasonable range and improved the osteogenic differentiation of bone mesenchymal stem cells compared with the other two scaffolds. In a rabbit femoral condyle defect model, the P500 group demonstrated unique performance in promoting new bone formation, indicating its great potential for use in bone defect regeneration therapy.

## 1. Introduction

The clinical treatment of large periarticular bone defects that are caused by trauma or tumor resection remains a major challenge [1]. Therefore, studies are increasingly focusing on approaches related to bone regeneration and natural bone replacement. Autograft techniques are considered to be the best option that is currently available, but limited sources of useful bone grafts and anatomical form mismatch restrict their large-scale application. In contrast, the use of allograft

increases the risk of immune rejection and pathogen transfer [2,3]. Some artificial bone materials, such as hydroxyapatite or tricalcium phosphate, can fill defects but lack durable mechanical strength [4,5].

Additive manufactured scaffolds have been used as an alternative material for bone defect repair, and these materials have received substantial attention. The use of customized porous implants allows the formation of patient-specific shapes and the precise control of topological parameters to promote bone ingrowth [6]. Bioinert metallic porous scaffolds, such as those made of titanium and its alloys, have achieved

Peer review under responsibility of KeAi Communications Co., Ltd.

\* Corresponding author. Department of Orthopedics, Peking University Third Hospital, Beijing, 100191, China.

\*\* Corresponding author.

\*\*\* Corresponding author.

E-mail address: [tiany@bjmu.edu.cn](mailto:tiany@bjmu.edu.cn) (Y. Tian).

<sup>1</sup> These authors contributed equally to this work.

<https://doi.org/10.1016/j.bioactmat.2023.06.009>

Received 13 April 2023; Received in revised form 30 May 2023; Accepted 16 June 2023

2452-199X/© 2023 The Authors. Publishing services by Elsevier B.V. on behalf of KeAi Communications Co. Ltd. This is an open access article under the CC BY-NC-ND license (<http://creativecommons.org/licenses/by-nc-nd/4.0/>).

desirable clinical effects [7]. Nevertheless, their permanent presence over time inhibits complete bone regeneration and may lead to implant-associated infections [8]. In addition to their biocompatibility, bone scaffolds should have at least the following characteristics: (i) they should have mechanical properties that support physical load during the bone repair period; (ii) they should have a highly porous and interconnected structure to promote bone ingrowth; and (iii) they should have good biodegradability to allow a final complete osseointegration.

Magnesium and its alloys are potential candidates for use in bone tissue engineering scaffolds because of their compatibility, osteoinductivity, biodegradability and mechanical properties. Magnesium is an essential mineral that is bioactive in beneficial enzymatic reactions and new bone formation [9,10]. The density and Young's modulus of magnesium and its alloys are similar to those of bone tissue, and magnesium and its alloys have been extensively investigated for use in orthopedic surgery [11]. The use of additive manufacturing magnesium alloy porous scaffolds with intricate internal architectures and adequate strength is a promising approach to overcome the challenges associated with complex external shapes and biodegradation [12,13].

Many studies have shown that the pore sizes of porous implants play a significant role in the movement of nutrients and cells. Larger pore sizes are more conducive to promoting blood supply and bone ingrowth; but the increasing pore size decreases the strength of the implant [14, 15]. Additionally, it must be acknowledged that pore size increases with scaffold degradation. The effects of pore size in additively manufactured magnesium on the mechanical properties and biodegradation as well as on new bone formation have rarely been reported. In this study, these characteristics were investigated using magnesium scaffolds with three distinct pore sizes, namely, 500, 800, and 1400  $\mu\text{m}$ .

## 2. Materials and methods

### 2.1. Personalized scaffold design and scaffold manufacturing

#### 2.1.1. Computer-aided design

Creo 7.0 (Parametric Technology Corporation, America) was used to design three distinct sheet gyroid scaffolds with the same porosity, namely, 60%. The distance between the two parallel struts was regarded as pore size in this paper. The measured pore size of P500, P800, and P1400 was 502.62  $\mu\text{m}$ , 789.51  $\mu\text{m}$ , and 1386.87  $\mu\text{m}$ , respectively. We discovered that the specific surface area of the scaffolds increased as the pore size decreased. The surface areas of the P500, P800, and P1400 scaffolds were 2425  $\text{mm}^2$ , 1663  $\text{mm}^2$ , and 1257  $\text{mm}^2$ , respectively.

#### 2.1.2. 3D printing and postprocessing

The scaffolds were made by a laser powder bed fusion machine (BLT S210, China). WE43 powder was prepared by centrifugal atomization (Tangshan Weihao, China). The powder included 3.71% Y, 2.21% Nd, 1.03% Gd, 0.37% Zr and residual Mg (by weight). These parameters were reported in previous studies [12]. The WE43 powder bed was preheated to 200 °C before melting. In the laser powder bed fusion (L-PBF) process, the chamber is filled with argon gas of over 99.99% purity to inhibit harmful reactions. Moreover, the oxygen concentration of the processing chamber is kept below 100 ppm. The following processing settings were used: a 60 W laser power, a 600 mm/s scanning speed, a 20  $\mu\text{m}$  layer thickness, and a 70  $\mu\text{m}$  hatch spacing. The scanning direction was rotated 67° between adjacent layers. The methods for the postprocessing treatment of the printed scaffolds were as follows. The scaffolds were chemically polished with 5% HCl, 5% HNO<sub>3</sub>, and residual C<sub>2</sub>H<sub>5</sub>OH (by volume) solution for 2 min and then ultrasonically cleaned in pure ethanol. To increase the corrosion resistance, the scaffolds were treated by high temperature oxidation (HTO) method. In a muffle furnace, the samples were heated at 525 °C in the presence of air for 8 h, and then were quenched in water.

### 2.2. Microstructural characterization and mechanical properties

#### 2.2.1. Scanning electron microscopy

The microstructures of the scaffolds were examined using a field emission scanning electron microscope (FESEM, HITACHI S-4800, Japan). Energy dispersive X-ray spectroscopy (EDS) was used to examine the chemical composition of areas of interest.

#### 2.2.2. Mechanical properties

A mechanical test was performed on cylindrical scaffolds (10\*10 mm) according to ISO 13314:2011. The scaffolds were compressed using a universal testing device at room temperature with a 0.5 mm/min speed and a 50% maximum strain. Both the yield strength and Young's modulus were calculated using the observed stress–strain curves.

### 2.3. In vitro degradation analysis

Immersion experiments were carried out in Hank's solution (37 °C, pH 7.4) and the exposure ratio was set as 20 mL/cm<sup>2</sup> in accordance with ASTM-G31-21 to evaluate the degradation behavior of the magnesium scaffolds with various pore sizes. Using inductively coupled plasma atomic emission spectroscopy (Leeman, USA), the magnesium content of the extracts was quantified. A pH meter was used to measure the pH levels of the extracts.

The magnesium scaffolds with various pore sizes underwent degradation, and the degradation behavior was characterized using micro-CT (Siemens INVEON MM, Germany). The micro-CT device parameters were as follows: 400  $\mu\text{A}$  tube current, 70 kV tube voltage, 400 ms exposure period, and 30  $\mu\text{m}$  scan resolution. 2D tomographic gray images of regions of interest (ROIs) were reconstructed by INVEON workplace (Siemens, Germany).

### 2.4. Cytocompatibility of BMSCs on sample extracts

#### 2.4.1. Cell adhesion

For cell adhesion analysis, a 50  $\mu\text{L}$  suspension of BMSCs ( $1 \times 10^4$  cells/well) was incubated on three groups of magnesium scaffolds with different pore sizes in 24-well culture plates. The cells were fixed in a 2.5% glutaraldehyde solution for an hour after 24 h of cell attachment. The samples were then dehydrated in gradient dilutions of alcohol and dried at room temperature. Finally, scanning electron microscopy was used to study cell morphology.

#### 2.4.2. Cytotoxicity

The samples were placed in DMEM supplemented with 10% fetal bovine serum (Gibco, USA), 100 units/mL penicillin (Gibco, USA), and 100 units/mL streptomycin (Gibco, USA) and incubated at 37 °C in an incubator (Thermo Fisher Scientific, USA) for 3 days to obtain the extracts. Then, we diluted the sample extracts to a specific concentration (10%). The measured Mg<sup>2+</sup> concentration of P500, P800, and P1400 was  $1.044 \pm 0.06688$  mM,  $2.090 \pm 0.1357$  mM, and  $2.820 \pm 0.05752$  mM. The sample extracts were used to culture bone marrow mesenchymal stem cells (BMSCs) at 37 °C in an incubator with 5% CO<sub>2</sub>.

We used the CCK-8 reagent (Yeasen, China) to assess cell viability and proliferation after 1, 3, and 5 days of culture. The absorbance of each well was measured at a 450 nm wavelength using a microplate reader (BioTek, Germany).

#### 2.4.3. Flow cytometry

Cells that had been cultured with various extracts for 7 days were trypsinized, centrifuged, and then resuspended in HEPES (pH 7.4) solution for analysis by flow cytometry. The cells were treated for 10–15 min at room temperature with 5  $\mu\text{L}$  of annexin V-FITC and 10  $\mu\text{L}$  of PI (Yeasen, China). Then, measurements were conducted using a flow cytometer (Beckman Coulter, USA).

#### 2.4.4. Live-dead assay

Cells were cultured with various extracts for 7 days, washed with standard phosphate-buffered saline (Solarbio, China), and then stained for 10 min with 2 mM calcein AM and 4 mM PI (Yeasen, China) in an incubator. Then, the cells were observed by fluorescence microscopy after gentle washing.

### 2.5. Osteogenic abilities of BMSCs treated with sample extracts

#### 2.5.1. Alkaline phosphatase (ALP) staining and quantification

To assess *in vitro* osteogenic capacity, BMSCs were seeded at a density of  $2 \times 10^4$  cells/cm<sup>2</sup> in 6-well plates. Once the cells reached approximately 70% confluence, we replaced the medium with diluted sample extracts supplemented with 50 mM ascorbic acid, 10 mM  $\beta$ -glycerophosphate and 100 nM dexamethasone (Sigma, USA). On day 14, the cultures were stained with BCIP/NBT solution (Solarbio, China) for ALP staining. The cells were lysed with lysis buffer, and P-nitrophenyl phosphate (pNpp) was added to the cell lysates and incubated for 20 min at 37 °C to produce p-nitrophenol, which has the strongest absorbance at 405 nm. The absorbance was measured by using a microplate reader (BioTek, Germany). A BCA kit (Yeasen, China) was used to quantify the total cellular protein concentrations for the normalization of ALP activity.

#### 2.5.2. Alizarin red staining and quantification

On day 21, Alizarin red staining (Sigma, USA) was performed to evaluate the formation of calcified nodules, and the staining intensity was measured using a microplate reader (BioTek, Germany) after adding 1% cetylpyridinium chloride extract (Sigma, USA) to dissolve the Alizarin red.

#### 2.5.3. Western blotting analysis of osteogenic marker expression

We used Western blotting analysis to assess the protein expression levels of runt-related transcription factor 2 (RUNX2), SP7 transcription factor 7 (SP7) and bone morphogenetic protein 2 (BMP-2). Equal amounts of proteins (20  $\mu$ g) were separated by sodium dodecyl sulfate-acrylamide gel electrophoresis (SDS-PAGE), and the separated proteins were then transferred to polyvinylidene difluoride membranes. The membranes were incubated with primary antibodies overnight at 4 °C after being blocked in TBST with 50 g/L skim milk powder for 2 h. The primary antibodies included rabbit anti-rat anti-RUNX2, monoclonal anti-SP7, anti-BMP2 (Abcam, UK) and polyclonal anti- $\beta$ -actin antibodies (Applygen, China). After three rounds of washing with TBST, the membranes were incubated with rabbit IgG secondary antibodies (Invitrogen, USA). An ECL detection kit was used to visualize the antigen-antibody complexes, and ImageJ was used to assess the signal intensities of the protein bands. And then we normalize the target protein/ $\beta$ -actin in Excel.

### 2.6. Osteogenic efficacy of magnesium scaffolds *in vivo*

#### 2.6.1. Surgical procedures

We utilized male New Zealand White rabbits that were 6 months old and weighed 3–3.5 kg. The surgical procedures were previously described. With an electric drill, a cylindrical defect that was 5 mm in diameter and 6 mm in depth was made on the lateral femoral condyle. We use sulfate calcium bone cement as the control group as it is the most commonly used biodegradable bone defect filler in clinical practice. The P1400 group, the P800 group, the P500 group, and the bone cement group were established from 20 rabbits divided equally into each group. Then, a scaffold that matched the defect was implanted.

#### 2.6.2. Postoperative radiological evaluation

Postoperative radiological evaluation was performed by C-arm fluoroscopy to show implant stability, loosening and associated complications. Rabbits were sacrificed 4 weeks after surgery. The following

experimental steps were performed after distal femur specimens were harvested. The femurs were preserved by incubation for 24 h at room temperature in 10% neutral formalin buffer. To assess bone regeneration and reconstruction, we scanned all the bone-scaffold compounds by using micro-CT (Siemens, Germany). The scanning settings were established as described above. The scaffold's inner space and bone growth were identified as the region of interest. 2D tomographic gray images of regions of interest (ROIs) were used for 3D reconstruction by INVEON workplace (Siemens, Germany). Trabecular parameters including bone volume over total volume (BV/TV), bone surface area/bone volume (BSA/BV), trabecular number (Tb.N), and trabecular separation (Th.Sp) were calculated with the INVEON workplace (Siemens, Germany).

#### 2.6.3. Histological evaluation

After successive dehydration using serial concentrations of ethanol, fixed femoral condyles were embedded in methyl methacrylate (MMA). For fluorescence microscopy and methylene blue/acid fuchsin staining, the MMA blocks were cut into 120- $\mu$ m sections and subsequently compressed to a thickness of 30–40  $\mu$ m.

### 2.7. Bioinformatics analysis of BMSCs treated with sample extracts

Transcriptomic analysis was conducted to investigate the mechanism by which extracts derived from P500 scaffolds affected BMSCs. After BMSCs reached 70% confluence, they were treated with sample extracts that had been diluted and supplemented with 50 mM ascorbic acid, 10 mM glycerophosphate, and 100 nM dexamethasone (Sigma, USA). To evaluate the transcriptome of the BMSCs, total RNA was collected on day 14, and high-throughput sequencing was performed. The molecular mechanisms by which the scaffold materials affected the BMSCs and the enriched signaling pathways were examined using Gene Ontology (GO) and Kyoto Encyclopedia of Genes and Genomes (KEGG) analyses.

### 2.8. Statistical analysis

In this study, experiments were conducted at least three times. All the experimental data were subjected to statistical analysis with SPSS 26.0 and are presented as histograms. Tukey's test was utilized for the post hoc comparison of several groups.  $P < 0.05$  was considered to be statistically significant.

## 3. Results and discussion

### 3.1. Microstructural characterization and mechanical properties

The pores in porous implants plays a crucial role in cell and nutrient transportation [16,17]. Porous metal scaffolds, such as titanium alloys and tantalum, have been shown to promote bone ingrowth and have been successfully utilized in clinical applications [18,19]. Chitosan, as a polymeric material, can also provide a porous scaffold that is conducive to cell-cell communication [20,21]. For bone tissue engineering scaffolds, the optimal pore size range is between 100 and 1000  $\mu$ m. In the field of additive manufacturing, porous topology design of undegradable metals are deeply studied. However, few studies have investigated additively manufactured biodegradable scaffolds with regards to pore topology design.

We first designed Gyroid scaffolds with different pore sizes, including P500, P800, and P1400, which had average pore sizes of 500  $\mu$ m, 800  $\mu$ m, and 1400  $\mu$ m, respectively, and a porosity of 60%. Gyroid structure has been verified to have excellent fluid permeability and mechanical properties, compare with traditional lattice porous structure [16–18]. Pore sizes of 500  $\mu$ m, 800  $\mu$ m, and 1400  $\mu$ m and a porosity of 60% were chosen based on the similarity of these parameters to the characteristics of natural bone tissue [22]. And all scaffolds was consistent with their CAD design models (Supplementary Fig. 1).

Currently, the degradation rate of magnesium alloys is mainly regulated by adjusting alloy composition and surface modification [23]. Common biomedical magnesium alloys such as Mg–Ca, Mg–Zn, and Mg–RE alloys can be controlled in their degradation rate by adjusting the composition of alloying elements [24]. Additionally, degradation rate regulation can also be achieved by preparing a corrosion-resistant coating on the magnesium alloy surface through various methods, including plasma electrolytic oxidation, electrochemical deposition, and ion implantation [25–30]. Furthermore, we have developed a high-temperature thermal oxidation technique to slow down the degradation rate of biomedical magnesium alloys, particularly suitable for additive manufactured Mg–RE alloys.

Fig. 1a–b presents the SEM images at the cross sections of L-PBF scaffolds and high temperature oxidation (HTO) scaffolds. L-PBF scaffolds exhibited a uniform microstructure. After HTO treatment, at the surface, the scaffolds formed a continuous oxide layer (I) with the enrichment of Y, Nd, Gd, Zr, and O, according to EDS analysis in (Fig. 1c). It separated the matrix from contact with fluids, therefore significantly increased the corrosion resistance of WE43. In addition, a

transition layer (II) appeared between the matrix and oxide layer because of the migration of Y. Fewer Mg–RE secondary phases existed in transition layer compared to the matrix (III), limiting the galvanic reaction.

We also examined the surface morphology of the magnesium alloy scaffolds with various pore diameters using scanning electron microscopy (SEM). The scaffold surfaces were smooth and dense with no visible defects, and the surface morphologies of the magnesium alloy scaffolds with different pore sizes were similar (Fig. 2b–d). Then, we used a universal testing apparatus to perform compression tests on the various scaffolds, and Fig. 2g shows the stress–strain curves of the various scaffolds with different pore sizes. The pore size had a significant effect on the compressive strength and elastic modulus of the scaffolds. According to the findings, the compressive strength and elastic modulus of the P500 group were 78.48 MPa and 1.22 GPa, those of the P800 group were 74.62 MPa and 1.11 GPa, and those of the P1400 group were 66.81 MPa and 1.03 GPa, respectively. It is also important to note that the compressive strength of all the scaffolds was similar to the mechanical characteristics of natural trabecular bone with the same

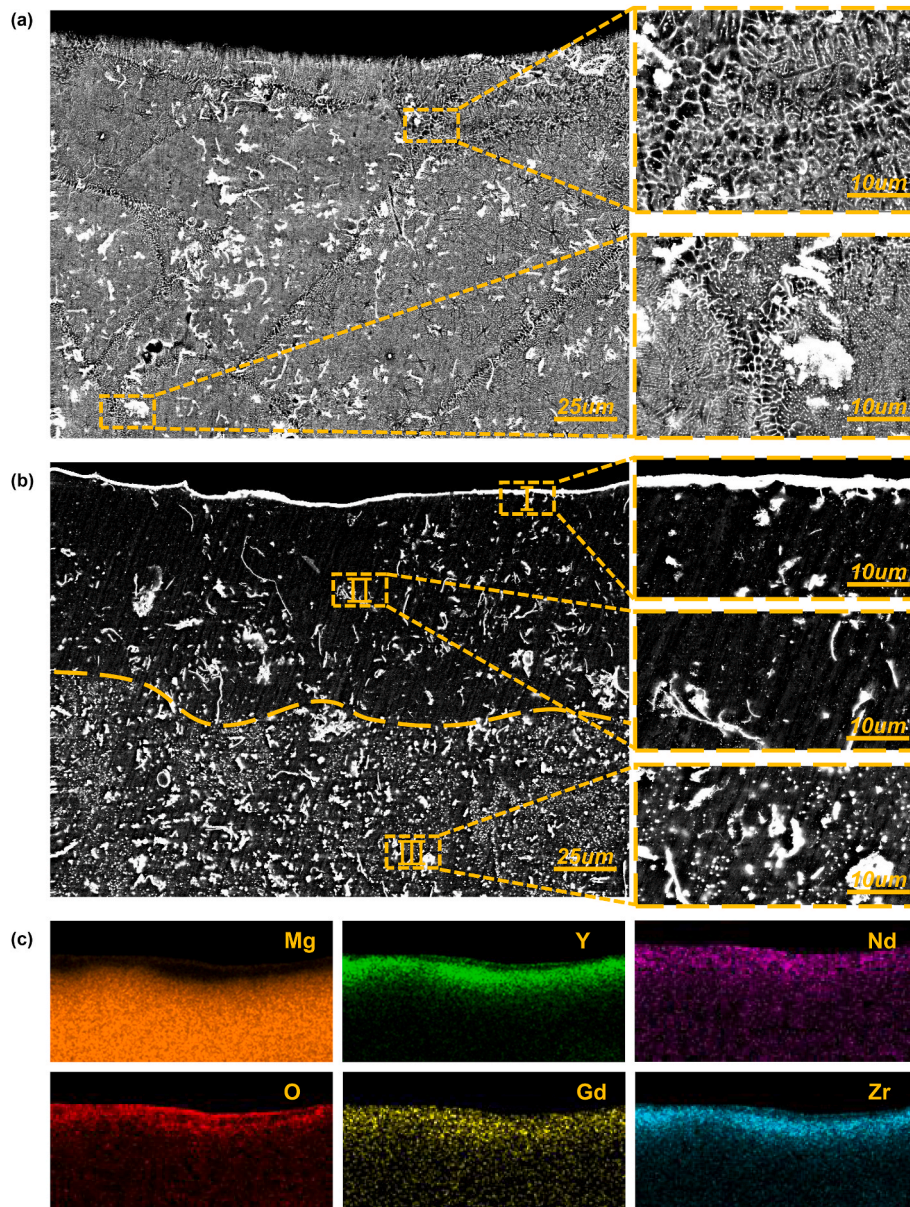
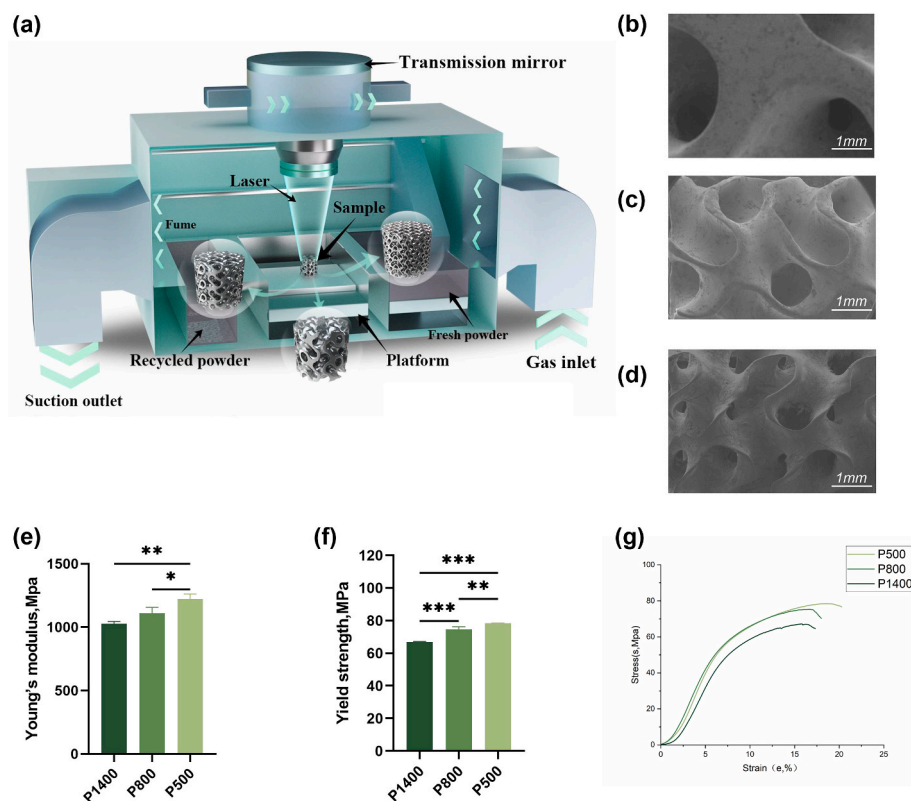


Fig. 1. (a–b) SEM images at the cross sections of the scaffolds with and without and HTO treatment, (c) EDS analysis at the oxide layer HTO scaffolds.



**Fig. 2.** (a) Fabrication of magnesium scaffolds using the L-PBF additive manufacturing technique. (b–d) Scanning electron microscopy (SEM) images of magnesium alloy scaffolds with varying pore sizes of 1400, 800, and 500  $\mu\text{m}$ . (e) Young's modulus, (f) compressive strength, and (g) stress-strain curves of the porous scaffolds with different pore sizes. Statistical significance is indicated by \* $p < 0.05$ , \*\* $p < 0.01$ , and \*\*\* $p < 0.001$ .

porosity (10–70 MPa) [22].

To make metal scaffolds suitable for the treatment of bone defects, their mechanical properties must match those of normal bone tissue to avoid limitations related to insufficient support strength or stress shielding [31].

### 3.2. *In vitro* degradation analysis

In this study, an *in vitro* degradation analysis was performed to evaluate the degradation behavior of the magnesium scaffolds with different pore sizes. Fig. 3a shows the morphology of the degradation products. After seven days of immersion, the scaffold surfaces were completely coated in degradation products. A few needle-shaped crystals also developed on the surface. EDS measurements were conducted on the area of interest, as shown in Supplementary Fig. 2. The degradation products on the scaffold surface were composed of  $\text{Mg}(\text{OH})_2$ . The surfaces of the scaffolds exhibited calcium and phosphorus enrichment, indicating the deposition of calcium phosphate [32,33].

The scaffolds were further observed after 7 days of degradation based on reconstructed micro-CT images. The degradation products loosely adhered to the pillar's surface. While only a tiny number of degradation products were observed on the outer layer, major degradation products were observed in the middle of the scaffolds (Fig. 3b).

Fig. 3c-d shows the release of magnesium ions and the pH value of the porous scaffolds at various time points. With prolonged incubation time, the amount of magnesium ions released and pH value continuously increased. The magnesium scaffolds with three different pore sizes exhibited different degradation rates. Generally, considerable increases in the degradation rate can be caused by greater surface areas [34]. Compared with the P800 and P1400 groups, the P500 group had a larger surface area that was exposed to the medium. Therefore, the amount of magnesium ions released and the pH value increased to a greater extent

in the P500 group than in the P800 and P1400 groups.

Therefore, the pore size is of significant importance for modulating the degradation behavior of additively manufactured porous magnesium.

### 3.3. Cytocompatibility of BMSCs treated with sample extracts

We further evaluated the adhesion of cells to the scaffolds using electron microscopy. BMSCs were directly seeded onto the HTO scaffolds in the P500, P800, and P1400 groups, as well as onto L-PBF (1400  $\mu\text{m}$  in pore size) scaffolds as a control. We found that BMSCs could adhere well to the surfaces of the HTO scaffolds in the P500, P800, and P1400 groups, extending pseudopodia and connecting with other cells. In contrast, the BMSCs seeded on the surface of the L-PBF sample contracted and detached, indicating relatively poor cell adhesion. Furthermore, we observed numerous corrosion cracks on the L-PBF sample surface, while no such cracks were observed on the surface of the HTO samples (Fig. 4a).

These findings may be attributed to the detrimental effects of excessive amounts of magnesium ions and hydrogen, which are generated by the rapid degradation of L-PBF samples, on cell viability and adhesion [35]. In contrast, the formation of an oxide layer on the surface of the HTO scaffolds inhibits the production of excessive amounts of magnesium ions and hydrogen. Moreover, rare earth oxide has a higher surface energy than pure magnesium, which is also favorable for cell adhesion [36].

The ISO 10993 standard-based cell toxicity test was initially developed for the analysis of nondegradable metals and polymers. An increasing amount of data suggests the possibility that these criteria are inappropriate for degradable magnesium alloys [37]. *In vivo*, magnesium and hydroxyls that are released are swiftly diluted by bodily fluids in the area and are quickly removed from circulation; these processes are

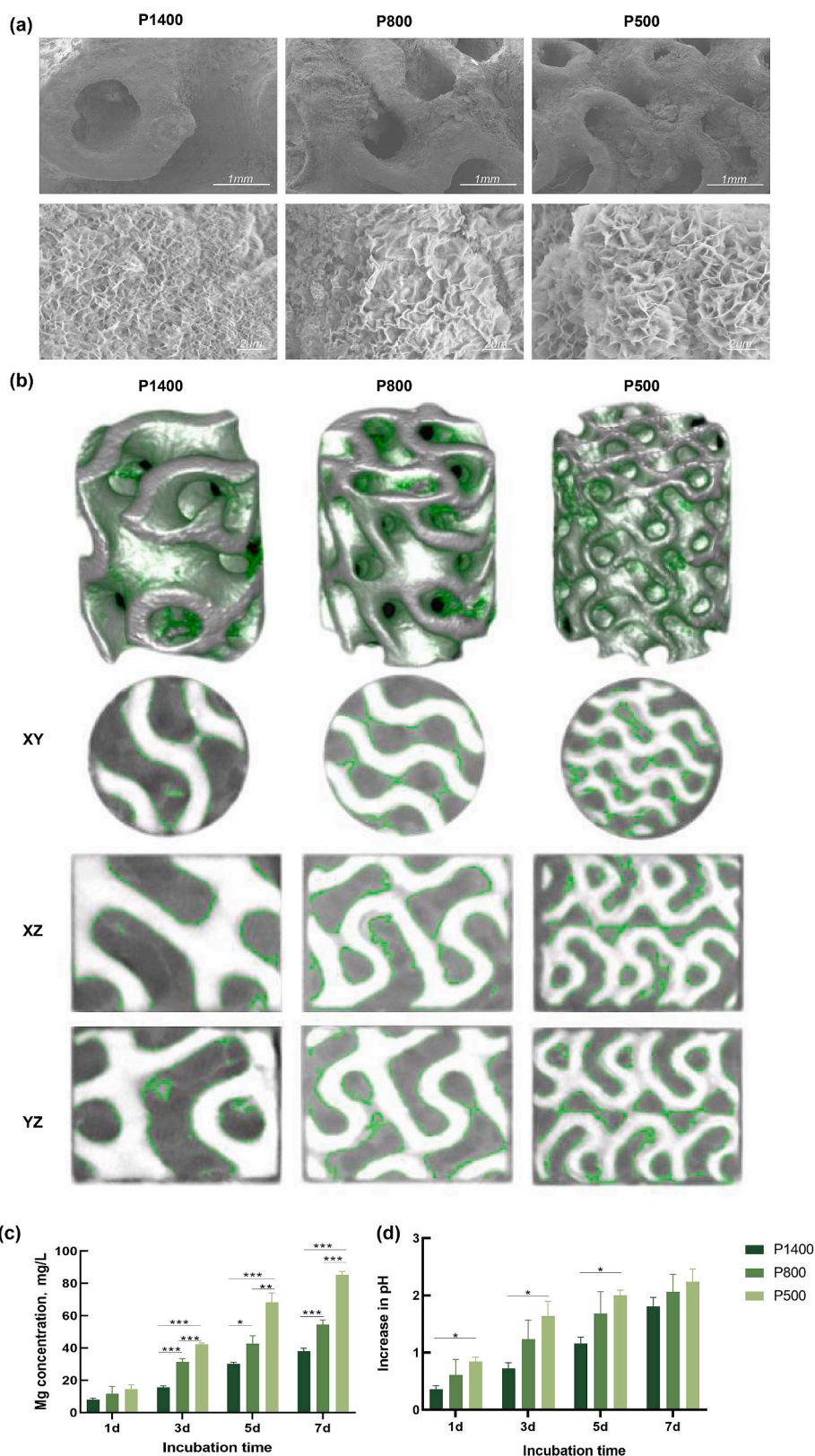


**Fig. 3.** (a) SEM image and (b) 3D reconstructed micro-CT images of the degradation products from the magnesium scaffolds with different pore sizes. (c) Magnesium ion release and (d) pH value changes of the porous scaffolds with different pore sizes. Statistical significance is indicated by \* $p < 0.05$ , \*\* $p < 0.01$ , and \*\*\* $p < 0.001$ .

poorly mimicked by *in vitro* environments. To better simulate *in vivo* conditions, we diluted extracts by 10 fold for use in the *in vitro* cell toxicity assay and *in vitro* osteogenic performance evaluation [38].

As shown in Fig. 4b, BMSCs were cultured in 10% extract for 7 days,

and live/dead staining demonstrated a wide distribution of cells with healthy spindle shapes. Quantitative cell counting showed that all the groups had at least 80% viable cells, and no statistically significant difference was observed among the groups (Fig. 4d). These results

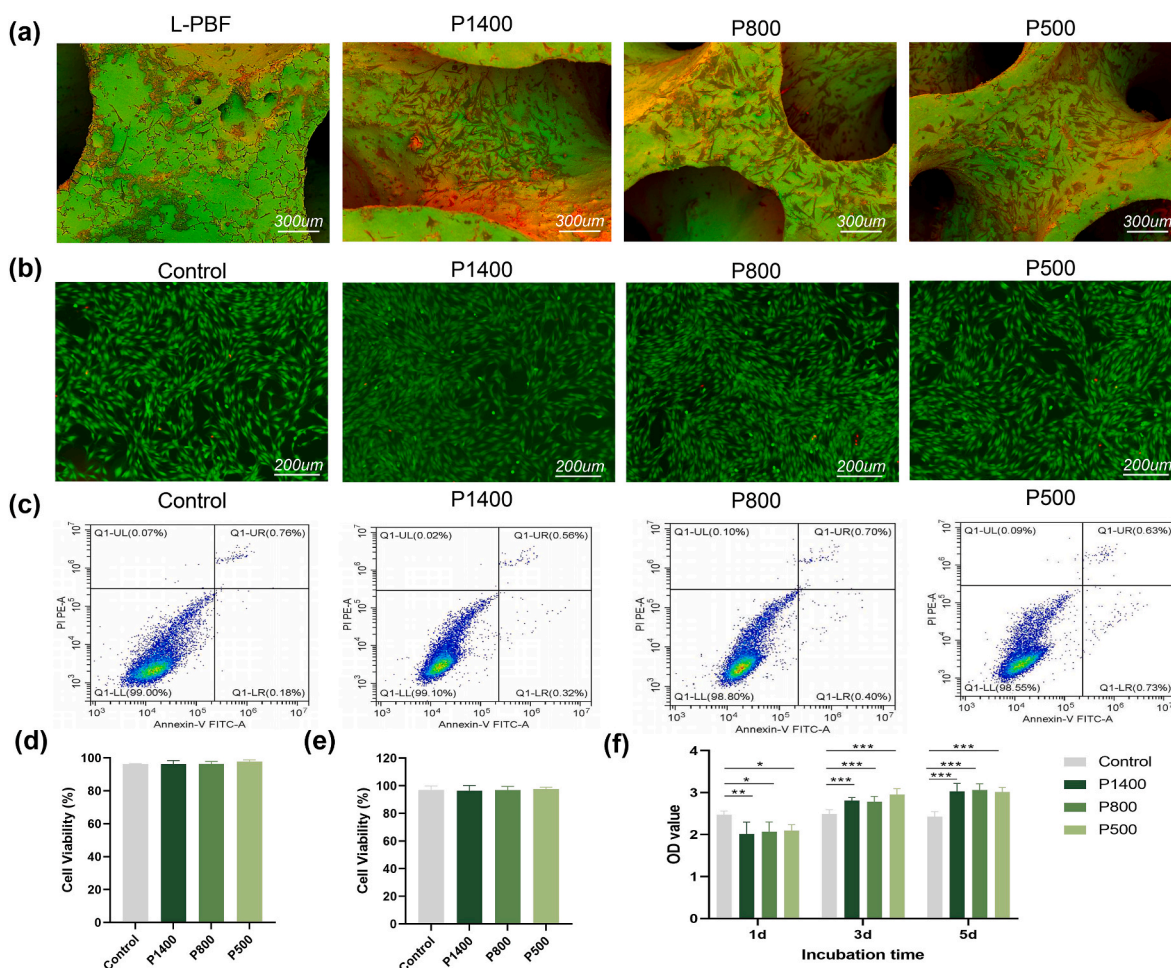


**Fig. 4.** (a) Morphology of bone marrow-derived mesenchymal stem cells (BMSCs) on the surface of L-PBF and heat-treated (HTO) scaffolds with varying pore sizes, as-built scaffolds were employed as a control. (b) Live/dead fluorescent staining and (c) apoptosis test of BMSCs after incubation for 7 days in scaffolds with varying pore sizes. (d–e) Statistical analysis of the proportion of viable cells in the live/dead fluorescent staining and apoptosis test. (f) Cell proliferation assay of BMSCs cultured in extracts for different periods. Statistical significance is indicated by \* $p < 0.05$ , \*\* $p < 0.01$ , and \*\*\* $p < 0.001$ .

indicate that the HTO scaffolds exhibit good biocompatibility.

As shown in Fig. 4c, flow cytometry analysis indicated that there was no significant decrease in cells that were not stained with annexin V and PI in the experimental groups compared to the control group. In the P500 group, 97.62% of the cells were unstained, while in the P800 and P1400 groups, 96.96% and 96.49% of the cells were unstained, respectively. The groups did not significantly differ from one another (Fig. 4e). To further quantify cell toxicity, the viability of BMSCs that were cultured in 10-fold diluted extracts was measured, and the results are shown in Fig. 4f. The cell viability in all the groups exceeded the cytotoxicity threshold ( $\geq 75\%$ ), indicating good cell compatibility, and there was no statistically significant difference among the groups.

To assess how different scaffold pore sizes affect BMSC osteogenic potential, we conducted *in vitro* osteogenic assessments by culturing BMSCs with sample extracts. ALP is a key player in osteoblast development and is an early indicator of osteogenesis, and ALP levels were first evaluated by staining and activity quantification [39,40]. The three sheet-gyroid scaffold groups (P500, P800, and P1400) showed larger ALP staining areas than the control group (Fig. 5a). On day 14, the P500 group further showed the largest staining area. Quantitatively, the staining area of the P500 group was twice that of the P1400 group and four times that of the control group on day 14 (Fig. 5b).

To evaluate the level of mineralization of the extracellular matrix (ECM) of BMSCs that were cultured on scaffolds with different pore sizes, Alizarin Red staining was performed, as it is a common method for

assessing ECM mineralization in cells or tissues [41,42]. The Alizarin Red staining results showed an increase in calcium nodule deposition in the P500, P800, and P1400 groups after 21 days of culture (Fig. 5c). Semiquantitative analysis of Alizarin Red staining using 1% cetylpyridinium chloride (Sigma) showed that the P500 group exhibited twice the amount of mineralization compared to the P1400 group after 21 days (Fig. 5d).

In addition, analysis of osteogenic protein expression in BMSCs, including osteogenic proteins such as RUNX-2, Sp7, and BMP-2, supported the view that magnesium alloy scaffolds can promote BMSC osteogenic differentiation (Fig. 5e–h). The findings demonstrated that magnesium alloy scaffolds efficiently enhanced BMSC osteogenic differentiation compared to the control group, with the P500 group showing the best effect due to its largest surface area.

### 3.4. Osteogenesis efficacy of magnesium scaffolds *in vivo*

To study the effects of the scaffolds with various structures on bone repair *in vivo*, we further established a rabbit femoral condyle defect model. Four types of implants were administered, including WE43 porous scaffolds with three different pore sizes (P500, P800, and P1400) and calcium sulfate bone cement as a control. During the experiment, all the rabbits exhibited normal behavior and similar activity. There were no observable signs of infection or inflammation.

One day following surgery, X-rays revealed that the experimental

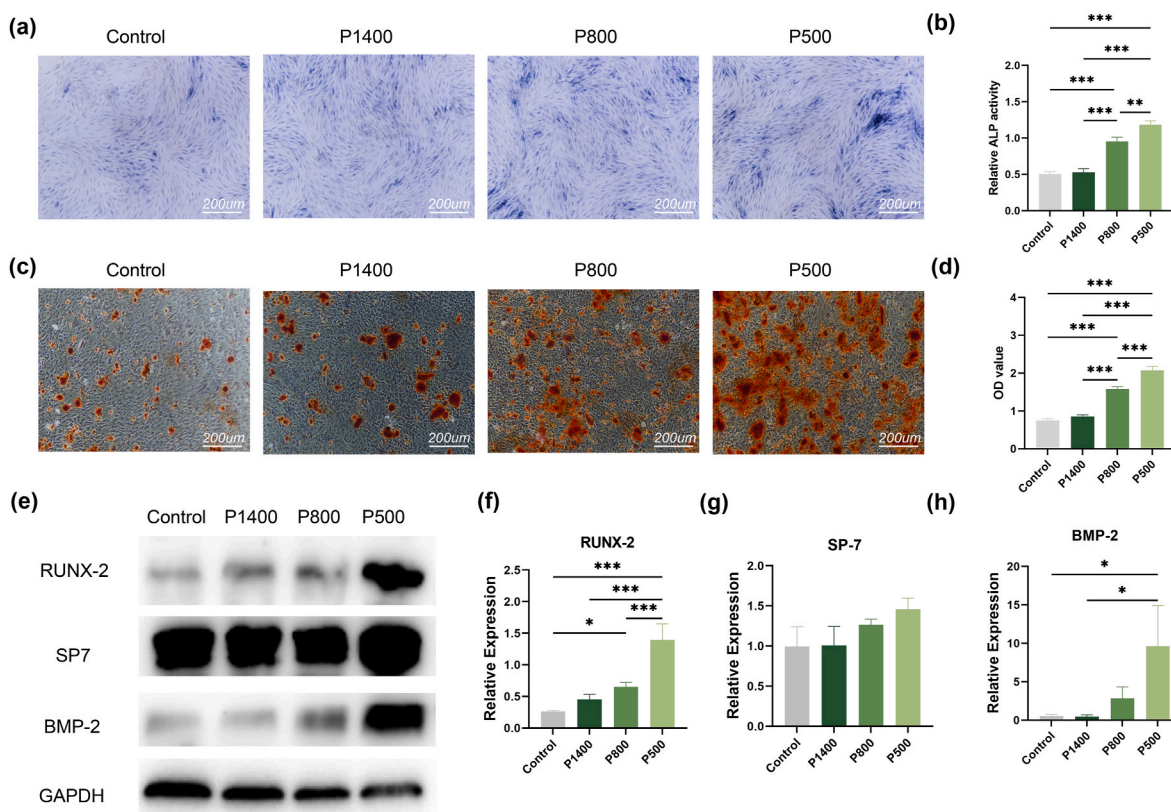


**Fig. 5.** (a) Alkaline phosphatase (ALP) staining and (b) ALP activity of BMSCs after 14 days of culture in extracts of scaffolds with varying pore sizes. (c) Alizarin red staining and (d) semi-quantitative analysis of mineralization after 21 days of culture. (e–h) Western blot results of the protein levels of RUNX-2, Sp7, and BMP-2 in BMSCs cultured in extracts for 14 days. Statistical significance is indicated by \* $p < 0.05$ , \*\* $p < 0.01$ , and \*\*\* $p < 0.001$ .

model had been successfully established. The WE43 porous scaffold structure was still clearly visible 4 weeks after surgery (Fig. 6a), indicating that the scaffold had not significantly degraded and had good structural integrity. In the bone cement group, the calcium sulfate bone cement disappeared, and no residual signs of the implant were observed. X-rays showed that all three magnesium alloy scaffold groups had high-density new tissue growing inside the defect, demonstrating progressive new bone regeneration.

Specimens were collected 4 weeks after implantation, and all the implants were found to be wrapped in soft tissue without obvious inflammation. Micro-CT reconstructions were used to evaluate new bone formation inside the scaffolds (Fig. 6b). More new bone was formed in the magnesium alloy scaffold group than in the control group. Statistical analysis further showed that the P500 group had significantly higher BV/TV, BSA/BV, and Tb.N values than the P800 and P1400 groups at 4 weeks after implantation (Fig. 6c–e), whereas the residual scaffold volume in the P1400 group was substantially greater than that in another two porous scaffold group (Fig. 6f).

The defect in the WE43 porous scaffold group was surrounded by more new bone, and some new bone was visually connected to the WE43 scaffold. In the bone cement group, more new bone was observed in the defect area than at 4 weeks, but the new bone was disordered, and most of the bone defect remained visually empty.

Methylene blue/acid fuchsin staining was performed at the defect site to better describe the osteogenic effect of the WE43 scaffold after surgery. After four weeks, the pores were filled with new bone, which further filled the bone defect region. Overall, the implanted WE43 porous scaffold demonstrated bone regeneration. However, the bone tissue was mainly immature woven bone, and well-reconstructed lamellar bone was not observed.

Calcein (green) were selected to label the newly formed bone. The magnesium alloy scaffold group had a significantly higher rate of bone

ingrowth than the control group, indicating that the magnesium alloy scaffold can promote new bone infiltration (Fig. 7). The amount of new bone tissue growth differed among the groups, and the P500 group had the highest amount of new bone tissue, indicating that the P500 scaffold had the best potential to support new bone formation (Fig. 8). These outcomes were consistent with the micro-CT results.

### 3.5. Bioinformatics analysis of BMSCs treated with sample extracts

Based on these results, we performed an RNA-seq analysis on the P500 group to further evaluate the effect of the sample extract on BMSC function and the underlying mechanism. The volcano plots showed that the mRNA expression patterns of the P500 group were obviously different from those of the control group, which indicated changes in the gene expression of BMSCs that were cultured with the extract derived from the P500 scaffolds. We used Gene Ontology (GO) and Kyoto Encyclopedia of Genes and Genomes (KEGG) analyses to study the activated functions and pathways. The GO analyses show that upregulated pathways in P500 group were actin cytoskeleton reorganization, apical plasma membrane and BMP signaling pathway, which are related to cytoskeleton reorganization, membrane structure assembly and osteogenic properties. KEGG enrichment analysis suggested that some upregulated terms, including the calcium signaling pathway, focal adhesion, ECM-receptor interaction and Wnt signaling pathway, were correlated with cytoskeleton reorganization and biomineralization. Interestingly, this result was consistent with the osteogenic protein expression in P500 group, including osteogenic proteins such as RUNX-2, Sp7, and BMP-2. Runx2 and Sp7 are considered as key nodes in the regulatory network of osteogenic differentiation [43]. Runx2 can promote the expression of major extracellular matrix proteins (including ALP, osteocalcin (OCN), osteopontin (OPN), and bone sialoprotein (BSP)) in chondrocytes and osteoblasts [44,45], and activate the

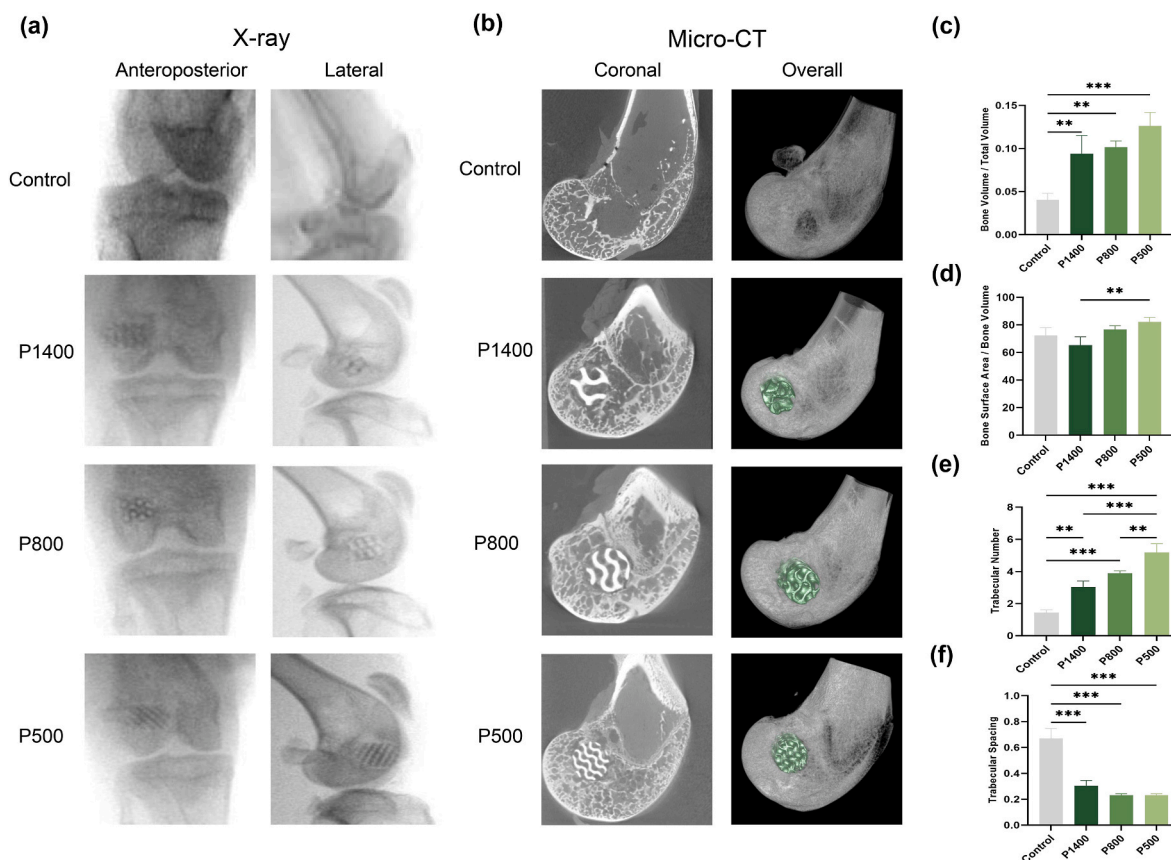


**Fig. 6.** (a) X-ray images and (b) micro-CT scans of the distal femur four weeks after implantation of the magnesium scaffolds with varying pore sizes, bone cement were employed as a control; trabecular parameters including (c) bone volume over total volume (BV/TV), (d) bone surface area/vone volume (BSA/BV), (e) trabecular number (Tb.N), and (f) trabecular separation (Tb.Sp). Statistical significance is indicated by \* $p < 0.05$ , \*\* $p < 0.01$ , and \*\*\* $p < 0.001$ .

expression of Sp7 [46]. Sp7 also drives the expression of extracellular matrix in osteoblasts [46,47]. BMP2 molecule plays an important role in inducing osteogenic differentiation. Previous literature has shown that RUNX2 is stabilized by BMP2-activated ERK/MAP kinase to promote osteoblast differentiation [48]. The canonical Wnt signaling pathway also acts on Runx2 to regulate osteogenic cell differentiation and bone formation [49]. Furthermore, the heatmap of the differentially expressed genes showed the upregulation of Mapk13, Tp53inp1 and Tlr4, which are also related to the process of bone regeneration.

#### 4. Conclusions

In this study, we found that high temperature oxidation improves the corrosion resistance of magnesium scaffold. And we successfully prepared WE43 magnesium alloy scaffolds with three different pore sizes (P500, P800, and P1400 groups). We discovered that the mechanical characteristics of the P500 scaffolds were much better than those of the other two scaffolds at the same porosity (60%). *In vitro* and *in vivo* investigations showed that the WE43 magnesium alloy scaffolds supported the survival of BMSCs and did not cause any local toxicity. Due to its larger specific surface area, the P500 scaffold released more magnesium ions within reasonable range and showed improved osteogenic differentiation of BMSCs compared with the other two groups. In a rabbit femoral condyle defect model, the P500 group demonstrated unique performance in promoting new bone formation, indicating its great potential for bone defect regeneration therapy.

#### Funding

This work was funded by the National Key Research and

Development Program of China (2018YFE0104200), the Youth Innovation Promotion Association CAS (2019031) and National Natural Science Foundation of China (51875310, 52175274, 82172065).

#### Ethics approval and consent to participate

All *in vivo* animal experiments were conducted according to the Institutional Animal Care and Use Committee at Peking University Third Hospital.

#### Consent for publication

Not applicable.

#### Availability of data

Not applicable.

#### CRediT authorship contribution statement

**Chaixin Wang:** Conceptualization, Investigation, Methodology, Validation, Funding acquisition, Writing – original draft. **Jinge Liu:** Conceptualization, Investigation, Methodology, Validation. **Shuyuan Min:** Investigation, Methodology, Validation. **Yu Liu:** Investigation, Methodology, Validation. **Bingchuan Liu:** Investigation, Methodology, Validation. **Yuanyu Hu:** Investigation, Methodology, Validation. **Zhenguang Wang:** Investigation, Methodology, Validation. **Fengbiao Mao:** Methodology, Validation. **Caimei Wang:** Methodology, Validation. **Xiaolin Ma:** Methodology, Validation. **Peng Wen:** Conceptualization, Supervision. **Yufeng Zheng:** Validation, Conceptualization,

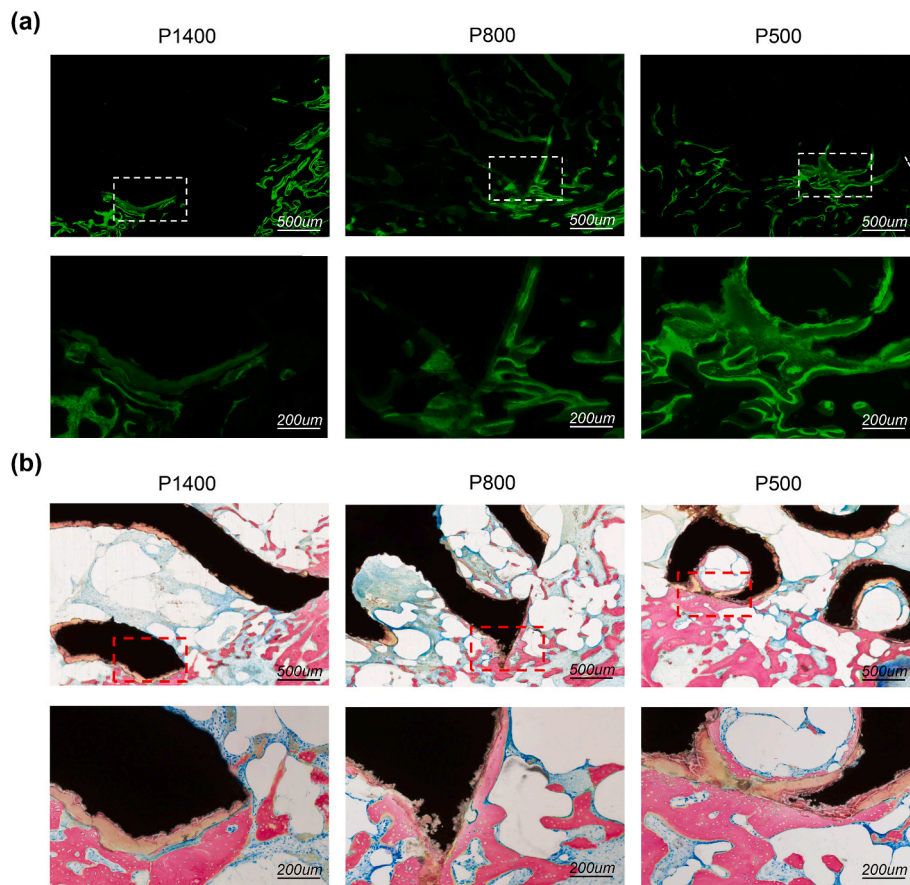


**Fig. 7.** (a) Representative fluorescence imaging and (b) methylene blue/acid fuchsin staining of the region of interest (ROI) at 4 weeks after implantation of the magnesium scaffolds with varying pore sizes.

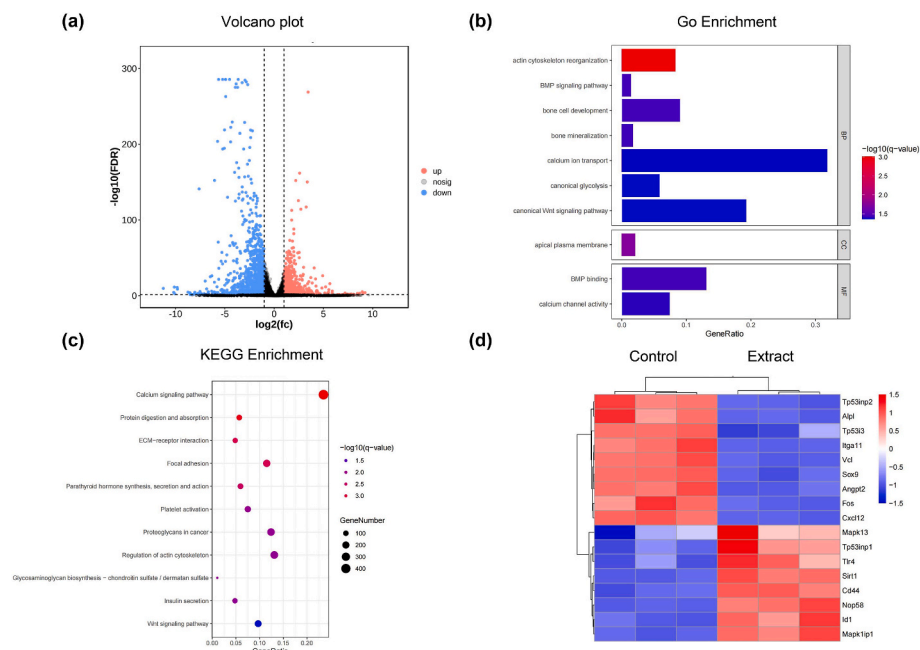


**Fig. 8.** (a) Volcano plots of mRNA expression characteristics of the P500 and control groups. (b) Gene ontology (GO) pathway analysis and (c) Kyoto Encyclopedia of Genes and Genomes (KEGG) pathway analysis of the gene expression changes of BMSCs with the sample extract of the P500 scaffolds. (d) Heatmap of differentially expressed genes between the P500 and control groups.

Funding acquisition, Supervision, Writing – review & editing. **Yun Tian:** Conceptualization, Funding acquisition, Supervision, Writing – review & editing.

### Declaration of competing interest

The authors declare that they have no known competing financial interests or personal relationships that could have appeared to influence the work reported in this paper.

### Acknowledgments

Not applicable.

### Appendix A. Supplementary data

Supplementary data to this article can be found online at <https://doi.org/10.1016/j.bioactmat.2023.06.009>.

### References

- [1] S. Van Bael, Y.C. Chai, S. Truscello, M. Moesen, G. Kerckhofs, H. Van Oosterwyck, J.-P. Kruth, J. Schrooten, The effect of pore geometry on the in vitro biological behavior of human periosteum-derived cells seeded on selective laser-melted Ti6Al4V bone scaffolds, *Acta Biomater.* 8 (2012) 2824–2834.
- [2] D.W. Huttmacher, Scaffolds in tissue engineering bone and cartilage, *Biomaterials* 21 (2000) 2529–2543.
- [3] S.T. Grambart, D.S. Anderson, T.D. Anderson, Bone grafting options, *Clin. Podiatr. Med. Surg.* 37 (2020) 593–600.
- [4] Y. Zhao, Z. Cui, B. Liu, J. Xiang, D. Qiu, Y. Tian, X. Qu, Z. Yang, An injectable strong hydrogel for bone reconstruction, *Adv Healthc Mater* 8 (2019), 1900709.
- [5] M. Šupová, Substituted hydroxyapatites for biomedical applications: a review, *Ceram. Int.* 41 (2015) 9203–9231.
- [6] F. Deng, L. Liu, Z. Li, J. Liu, 3D printed Ti6Al4V bone scaffolds with different pore structure effects on bone ingrowth, *J. Biol. Eng.* 15 (2021) 1–13.
- [7] S.H. Jariwala, G.S. Lewis, Z.J. Bushman, J.H. Adair, H.J. Donahue, 3D printing of personalized artificial bone scaffolds, *3D Print. Addit. Manuf.* 2 (2015) 56–64.
- [8] I.A.J. van Hengel, M. Riool, L.E. Fratila-Apachitei, J. Witte-Bouma, E. Farrell, A. A. Zadpoor, S.A.J. Zaat, I. Apachitei, Selective laser melting porous metallic implants with immobilized silver nanoparticles kill and prevent biofilm formation by methicillin-resistant *Staphylococcus aureus*, *Biomaterials* 140 (2017) 1–15.
- [9] Y. Zhang, J. Xu, Y.C. Ruan, M.K. Yu, M. O’Laughlin, H. Wise, D. Chen, L. Tian, D. Shi, J. Wang, Implant-derived magnesium induces local neuronal production of CGRP to improve bone-fracture healing in rats, *Nat. Med.* 22 (2016) 1160–1169.
- [10] J. Zhang, Y. Jiang, Z. Shang, B. Zhao, M. Jiao, W. Liu, M. Cheng, B. Zhai, Y. Guo, B. Liu, Biodegradable metals for bone defect repair: a systematic review and meta-analysis based on animal studies, *Bioact. Mater.* 6 (2021) 4027–4052.
- [11] M.P. Staiger, A.M. Pietak, J. Huadmai, G. Dias, Magnesium and its alloys as orthopedic biomaterials: a review, *Biomaterials* 27 (2006) 1728–1734.
- [12] J. Liu, B. Liu, S. Min, B. Yin, B. Peng, Z. Yu, C. Wang, X. Ma, P. Wen, Y. Tian, Biodegradable magnesium alloy WE43 porous scaffolds fabricated by laser powder bed fusion for orthopedic applications: process optimization, in vitro and in vivo investigation, *Bioact. Mater.* 16 (2022) 301–319.
- [13] K. Xie, N. Wang, Y. Guo, S. Zhao, J. Tan, L. Wang, G. Li, J. Wu, Y. Yang, W. Xu, Additively manufactured biodegradable porous magnesium implants for elimination of implant-related infections: an in vitro and in vivo study, *Bioact. Mater.* 8 (2022) 140–152.
- [14] V. Karageorgiou, D. Kaplan, Porosity of 3D biomaterial scaffolds and osteogenesis, *Biomaterials* 26 (2005) 5474–5491.
- [15] H. Hornberger, S. Virtanen, A.R. Boccaccini, Biomedical coatings on magnesium alloys—a review, *Acta Biomater.* 8 (2012) 2442–2455.
- [16] B. Otsuki, M. Takemoto, S. Fujibayashi, M. Neo, T. Kokubo, T. Nakamura, Pore throat size and connectivity determine bone and tissue ingrowth into porous implants: three-dimensional micro-CT based structural analyses of porous bioactive titanium implants, *Biomaterials* 27 (2006) 5892–5900.
- [17] V. Karageorgiou, D. Kaplan, Porosity of 3D biomaterial scaffolds and osteogenesis, *Biomaterials* 26 (2005) 5474–5491.
- [18] K.C. Nune, R.D.K. Misra, S.J. Li, Y.L. Hao, R. Yang, Osteoblast cellular activity on low elastic modulus Ti–24Nb–4Zr–8Sn alloy, *Dent. Mater.* 33 (2017) 152–165.
- [19] S.J. Li, X.K. Li, W.T. Hou, K.C. Nune, R.D.K. Misra, V.L. Correa-Rodriguez, Z. Guo, Y.L. Hao, R. Yang, L.E. Murr, Fabrication of Open-Cellular (Porous) Titanium Alloy Implants: Osseointegration, Vascularization and Preliminary Human Trials, 2018.
- [20] M. Bayindir Bilgic, N.T. Lacin, H. Berber, B. Mansuroglu, In vitro evaluation of alpha-tocopherol loaded carboxymethylcellulose chitosan copolymers as wound dressing materials, *Mater. Technol.* 34 (2019) 386–393.
- [21] X. Gu, R. Cao, Y. Li, S. Liu, Z. Wang, S. Feng, F. Li, S. Lyu, Three-component antibacterial membrane of poly (butylene carbonate), poly (lactic acid) and chitosan prepared by electrospinning, *Mater. Technol.* 34 (2019) 463–470.
- [22] S.A. Goldstein, D.L. Wilson, D.A. Sonstegard, L.S. Matthews, The mechanical properties of human tibial trabecular bone as a function of metaphyseal location, *J. Biomech.* 16 (1983) 965–969.
- [23] D. Zhao, F. Witte, F. Lu, J. Wang, J. Li, L. Qin, Current status on clinical applications of magnesium-based orthopaedic implants: a review from clinical translational perspective, *Biomaterials* 112 (2017) 287–302.
- [24] G. Uppal, A. Thakur, A. Chauhan, S. Bala, Magnesium based implants for functional bone tissue regeneration—A review, *J. Magnesium Alloys* 10 (2022) 356–386.
- [25] F. Benn, N. Kröger, M. Zinser, K. van Gaalen, T.J. Vaughan, M. Yan, R. Smeets, E. Bibiza, S. Malinov, F. Buchanan, Influence of surface condition on the degradation behaviour and biocompatibility of additively manufactured WE43, *Mater. Sci. Eng. C* 124 (2021), 112016.
- [26] A. Kopp, T. Derra, M. Mütter, L. Jauer, J.H. Schleifenbaum, M. Voshage, O. Jung, R. Smeets, N. Kröger, Influence of design and postprocessing parameters on the degradation behavior and mechanical properties of additively manufactured magnesium scaffolds, *Acta Biomater.* 98 (2019) 23–35.
- [27] R.B. Heimann, Magnesium alloys for biomedical application: Advanced corrosion control through surface coating, *Surf. Coat. Technol.* 405 (2021), 126521.
- [28] K. Rendenbach, H. Fischer, A. Kopp, K. Schmidt-Bleek, H. Kreiker, S. Stumpp, M. Thiele, G. Duda, H. Hanken, B. Beck-Broichsitter, Improved in vivo osseointegration and degradation behavior of PEO surface-modified WE43 magnesium plates and screws after 6 and 12 months, *Mater. Sci. Eng. C* 129 (2021), 112380.
- [29] J. Chen, Y. Yang, I.P. Etim, L. Tan, K. Yang, R.D.K. Misra, J. Wang, X. Su, Recent advances on development of hydroxyapatite coating on biodegradable magnesium alloys: a review, *Materials* 14 (2021) 5550.
- [30] A. Mahapatro, T.D. Matos Negron, A.S. Gomes, Nanostructured self assembled monolayers on magnesium for improved biological performance, *Mater. Technol.* 31 (2016) 818–827.
- [31] R. Karunakaran, S. Orgies, A. Tamayol, F. Bobaru, M.P. Sealy, Additive manufacturing of magnesium alloys, *Bioact. Mater.* 5 (2020) 44–54, <https://doi.org/10.1016/j.bioactmat.2019.12.004>.
- [32] F. Benn, N. Kröger, M. Zinser, K. van Gaalen, T.J. Vaughan, M. Yan, R. Smeets, E. Bibiza, S. Malinov, F. Buchanan, Influence of surface condition on the degradation behaviour and biocompatibility of additively manufactured WE43, *Mater. Sci. Eng. C* 124 (2021), 112016.
- [33] A. Kopp, T. Derra, M. Mütter, L. Jauer, J.H. Schleifenbaum, M. Voshage, O. Jung, R. Smeets, N. Kröger, Influence of design and postprocessing parameters on the degradation behavior and mechanical properties of additively manufactured magnesium scaffolds, *Acta Biomater.* 98 (2019) 23–35.
- [34] A.P. Md Saad, A.T. Prakoso, M.A. Sulong, H. Basri, D.A. Wahjuningrum, A. Syahrom, Impacts of dynamic degradation on the morphological and mechanical characterisation of porous magnesium scaffold, *Biomech. Model. Mechanobiol.* 18 (2019) 797–811.
- [35] L. Wu, F. Feyerabend, A.F. Schilling, R. Willumeit-Römer, B.J.C. Luthringer, Effects of extracellular magnesium extract on the proliferation and differentiation of human osteoblasts and osteoclasts in coculture, *Acta Biomater.* 27 (2015) 294–304.
- [36] Y. Zhang, X. Xu, Machine learning modeling of metal surface energy, *Mater. Chem. Phys.* 267 (2021), 124622.
- [37] D. Zhao, F. Witte, F. Lu, J. Wang, J. Li, L. Qin, Current status on clinical applications of magnesium-based orthopaedic implants: a review from clinical translational perspective, *Biomaterials* 112 (2017) 287–302.
- [38] J. Fischer, D. Pröfrock, N. Hort, R. Willumeit, F. Feyerabend, Improved cytotoxicity testing of magnesium materials, *Mater. Sci. Eng., B* 176 (2011) 830–834, <https://doi.org/10.1016/j.mseb.2011.04.008>.
- [39] H.-J. Prins, A.K. Braat, D. Gawlitza, W.J.A. Dhert, D.A. Egan, E. Tijssen-Slump, H. Yuan, P.J. Coffer, H. Rozemuller, A.C. Martens, In vitro induction of alkaline phosphatase levels predicts in vivo bone forming capacity of human bone marrow stromal cells, *Stem Cell Res.* 12 (2014) 428–440.
- [40] S. Vimalraj, Alkaline phosphatase: structure, expression and its function in bone mineralization, *Gene* 754 (2020), 144855.
- [41] P. Zhuang, X. Wu, H. Dai, Y. Yao, T. Qiu, Y. Han, S. Li, Nano  $\beta$ -tricalcium phosphate/hydrogel encapsulated scaffolds promote osteogenic differentiation of bone marrow stromal cells through ATP metabolism, *Mater. Des.* 208 (2021), 109881.
- [42] A. Klymov, J. Song, X. Cai, J. Te Riet, S. Leeuwenburgh, J.A. Jansen, X. F. Walboomers, Increased acellular and cellular surface mineralization induced by nanogrooves in combination with a calcium-phosphate coating, *Acta Biomater.* 31 (2016) 368–377.
- [43] T. Komori, Regulation of osteoblast differentiation by transcription factors, *J. Cell. Biochem.* 99 (2006) 1233–1239.
- [44] P. Ducy, R. Zhang, V. Geoffroy, A.L. Ridall, G. Karsenty, *Osf2/Cbfa1*: a transcriptional activator of osteoblast differentiation, *Cell* 89 (1997) 747–754.
- [45] C. Banerjee, L.R. McCabe, J. Choi, S.W. Hiebert, J.L. Stein, G.S. Stein, J.B. Lian, Runt homology domain proteins in osteoblast differentiation: *AML3/CBFA1* is a major component of a bone-specific complex, *J. Cell. Biochem.* 66 (1997) 1–8.
- [46] K. Nakashima, X. Zhou, G. Kunkel, Z. Zhang, J.M. Deng, R.R. Behringer, B. De Crombrughe, The novel zinc finger-containing transcription factor *osterix* is required for osteoblast differentiation and bone formation, *Cell* 108 (2002) 17–29.

- [47] T. Matsubara, K. Kida, A. Yamaguchi, K. Hata, F. Ichida, H. Meguro, H. Aburatani, R. Nishimura, T. Yoneda, Bmp2 regulates osterix through msx2 and runx2 during osteoblast differentiation, *J. Biol. Chem.* 283 (2008) 29119–29125.
- [48] J.H. Jun, W.-J. Yoon, S.-B. Seo, K.-M. Woo, G.-S. Kim, H.-M. Ryoo, J.-H. Baek, BMP2-activated Erk/MAP kinase stabilizes Runx2 by increasing p300 levels and histone acetyltransferase activity, *J. Biol. Chem.* 285 (2010) 36410–36419.
- [49] T.P. Hill, D. Später, M.M. Taketo, W. Birchmeier, C. Hartmann, Canonical Wnt/ $\beta$ -catenin signaling prevents osteoblasts from differentiating into chondrocytes, *Dev. Cell* 8 (2005) 727–738.